

Evaluation of Inverse Algorithms in the Analysis of Magnetic Flux Leakage Data

Jens Haeuise, Ralf Unger, Thomas Beuker, and Matthias E. Bellemann

Abstract—We evaluate the use of linear and nonlinear inverse algorithms (maximum entropy method, low resolution electromagnetic tomography, L_1 and L_2 norm methods) in the analysis of magnetic flux leakage (MFL) measurements commonly used for the detection of flaws and irregularities in gas and oil pipelines. We employed MFL data from a pipe with well-defined artificial surface breaking flaws at the internal and external wall. Except for the low-resolution electromagnetic tomography, all algorithms show, on average, similar accuracy in the flaw extent estimation. Maximum entropy and the L_1 norm have a tendency to yield better results for smaller flaws, while the L_2 norm performs slightly better for larger flaws. The errors of the flaw location estimation are comparable for the maximum entropy and the L_2 norm algorithm. The L_1 norm performs worse for those flaws situated on the internal pipe wall. Linear methods (L_2 norm) are easier to implement and require less computation time than nonlinear methods (maximum entropy method, L_1 norm). In conclusion, inverse algorithms potentially provide a powerful means for the detection and characterization of flaws in MFL data.

Index Terms—Inverse problems, magnetic flux leakage, nondestructive testing, pipeline inspection.

I. INTRODUCTION

MONITORING of gas and oil pipelines is of crucial importance for various technical and economical reasons, especially the detection of flaws and irregularities is an important task in pipeline maintenance. As those flaws are often situated in inaccessible regions, it is not possible to perform a visual inspection. Therefore, inline inspection vehicles are used, which are pumped through the pipeline together with the oil and gas flow. The magnetic flux leakage (MFL) method is a technique used for the detection of flaws in metal sheets or pipes for more than 70 years [1].

The basic principle of the MFL method is illustrated in Fig. 1. A static, uniform magnetic field is coupled into the permeable wall of the pipeline. Flaws in the pipe wall generate magnetic field perturbations which are called leakage fields when they leak out of the pipe. The MFL technique is commonly used in the inline inspection business. The above mentioned autonomous vehicles are equipped with MFL units and onboard computers to register and store the magnetic field patterns of the inspected steel pipe while traveling in the pipeline. The

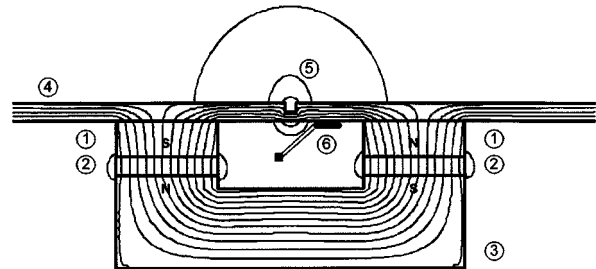


Fig. 1. Schematic operation of the magnetic flux leakage method: ① steel brush, ② permanent magnet, ③ soft iron yoke, ④ pipe wall, ⑤ metal loss flaw causing stray flux, which is measured by ⑥ magnetic field sensors mounted on a support. The device moves into the left direction on the drawing.

measured leakage of the magnetic flux is analyzed afterwards off-line in order to extract the location, the extent, and the depth of flaws in the pipe wall.

The analysis of MFL data involves the solution of the forward problem (i.e., the computation of the field from given sources and geometry) and the solution of the inverse problem (i.e., the estimation of source parameters or geometries from given magnetic field data). For the solution of the forward problem, both analytical (e.g., [2]–[4]) and numerical methods (e.g., [5]–[7]), have been employed in the past. Solutions of the inverse problem can be classified into the application of: 1) direct, analytic parameter estimations; 2) nonlinear search algorithms [7]; 3) linear estimation techniques [8]–[11]; and 4) filter techniques (projection or de-blurring methods) [12]. Recently, sophisticated forward models and inversion techniques have been developed (e.g., [13]–[15]).

The goal of this paper is the application and evaluation of different inverse algorithms based on linear and nonlinear estimation techniques in the field of MFL data analysis.

II. MATERIALS AND METHODS

A. MFL Data

In order to mathematically describe the pipe, we define a cylindrical coordinate system (φ, ρ, z) , where φ depicts the circumferential direction of the pipe (angle), ρ the radial direction of the pipe (radius), and z the axial direction of the pipe. Since the pipe has a fixed diameter, we give the dimensions along the circumferential direction also in millimeters.

Measurements were carried out at the inside surface of a pipe using the principle technique described in Fig. 1 on a set of circular flaws (flat bottom holes) in a pipe wall (inner diameter of the pipe = 610 mm; wall thickness = 20 mm). The holes had the following parameters: flaw diameter = 5, 10, 16, 24, or

Manuscript received March 5, 2001; revised December 12, 2001.

J. Haeuise and R. Unger are with the Biomagnetic Center, Friedrich-Schiller-University, 07743 Jena, Germany (e-mail: haeuise@biomag.uni-jena.de).

T. Beuker is with the R&D Department, H.ROSEN Engineering Ltd., 49811 Lingen (Ems), Germany.

M. E. Bellemann is with the Department of Biomedical Engineering, University of Applied Sciences, 07745 Jena, Germany.

Publisher Item Identifier S 0018-9464(02)03635-X.

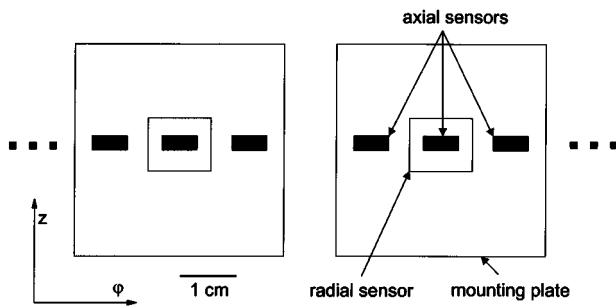


Fig. 2. Sensor geometry and cylindrical coordinate system (z axial direction, φ circumferential direction, ρ radial direction pointing into the drawing plane).

36 mm; flaw position = inside or outside the pipe wall; and flaw depth = 20% or 50% of the wall thickness.

For the detection of the stray field, a commercial device with two different types of sensors were used simultaneously (Fig. 2): a Hall sensor measured the axial magnetic field (in the following indicated by B_z) and a coil sensor measured the axial derivative of the radial magnetic field component (in the following indicated by B_ρ). Please note that the measurement principle (measured quantities) is different for the two sensor types. The sensor geometry is given in Fig. 2. The distance between the Hall sensors and the pipe wall was 3.5 mm, and the distance between the coil sensors and the pipe wall was 6 mm.

For the inverse computations, we assumed stationarity (see also below) and we restricted the number of measuring points included in each inverse computation so that this number was as small as possible (reduced computation time) while still covering all relevant field information. This yielded an area of 106 mm in circumferential direction and 72 mm in axial direction, including 108 radial and 324 axial measuring points (Fig. 3).

B. Normalization

An estimate of the noise present in the data was obtained from channels containing no visible signal. The standard deviation σ was employed to quantify the amount of noise. In the next step, all data were transformed into the signal-to-noise space by dividing all values by σ . This transformation simplifies the use of data sets with different orders of magnitude (here B_z and B_ρ) in inverse algorithms. The signal-to-noise ratio (SNR) was determined by

$$\text{SNR} = \frac{1}{\sigma} \frac{1}{N} \left(\sum_{i=1}^N X_{\max}^i - \sum_{j=1}^N X_{\min}^j \right) \quad (1)$$

where N is set to 10 and, thus, X_{\max}^i and X_{\min}^j indicate the ten largest and ten smallest values, respectively. Fig. 4 gives the SNR values for all flaws.

The SNR values for B_ρ were found to be significantly larger than the values for B_z . All values for B_ρ were above 11, except for the two flaws with the smallest signals (diameter 5 mm, position outside, depth 20% and 50%) which were excluded from further analysis. All other flaws were used throughout the paper. The better the SNR, the better the source localization accuracy. Commonly, SNR values of 10 and above are sufficient for a source localization accuracy of single dipoles of about 5 mm

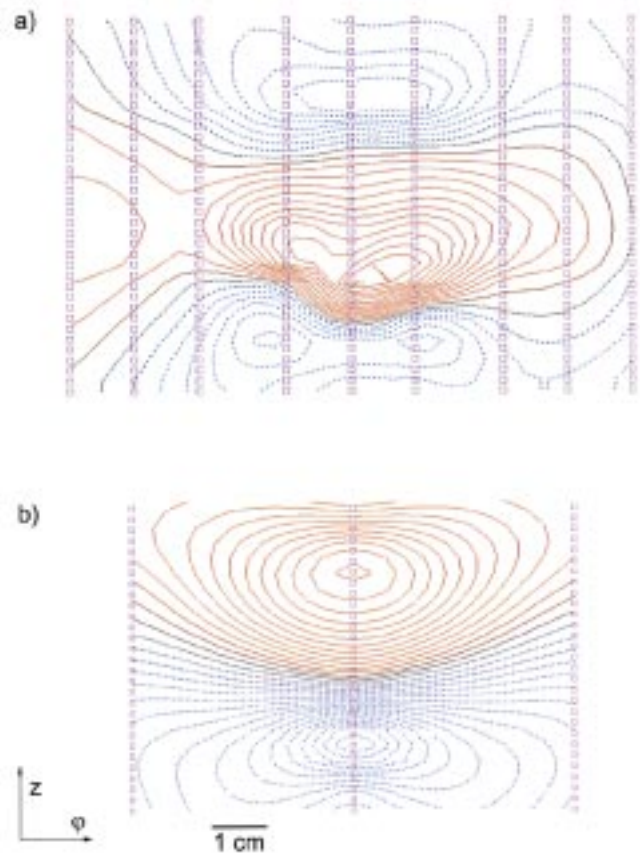


Fig. 3. Magnetic field profiles of an internal flaw (diameter 36 mm, 50% wall thickness) measured with the (a) axial and (b) radial magnetic field sensors. Sensor locations are depicted by squares. Same scaling in (a) and (b).

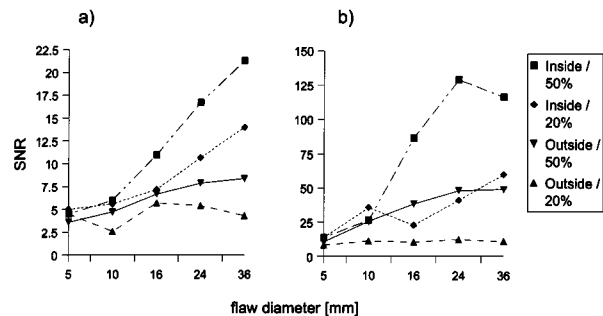


Fig. 4. Calculated SNR of (a) B_z and (b) B_ρ of each flaw. Please note the different scaling in (a) and (b). Squares indicate flaws with a depth of 50% wall thickness on the inside wall, diamonds indicate flaws with a depth of 20% wall thickness on the inside wall, downward pointing triangles indicate flaws with a depth of 50% wall thickness on the outside wall, and upward pointing triangles indicate flaws with a depth of 20% wall thickness on the outside wall.

on average [16]. Please note that the transformation into the signal-to-noise space was performed separately for the B_ρ and the B_z components.

C. Forward Solution

The current sheet convention and the pole sheet convention are two approaches used in computational methods in magnetostatics [17], [18]. The current sheet convention employs currents (often line-like current elements) to approximate the magnetic field produced by a magnetized body while the pole

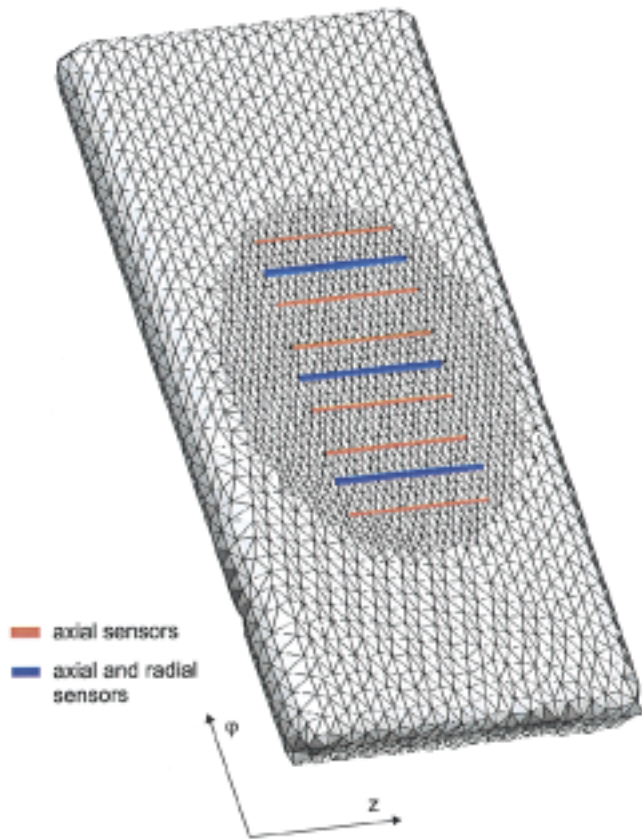


Fig. 5. BEM model and position of the sensors. Only the principal position of the sensors is depicted. Please see Fig. 2 for a detailed sensor representation with correct sizes. Note the local mesh refinement below the position of the measuring points.

sheet convention does so with the help of a pole density. Using the analogy of the current sheet model, we solve the forward problem in this study. Line-like current elements can generally be approximated by current dipoles. The sources of the magnetic stray field were modeled employing a sheet of electric current dipoles in an electric volume conductor. Although this approach is not straightforward and has not been described in the literature dealing with magnetic flux leakage problems so far, it is common in other fields of electromagnetic field computation [17]–[19]. We have chosen this approach because of the software available. Other approaches (even simpler ones) are possible as well.

A piece of pipe wall was modeled with the help of the boundary-element method (BEM). A total of 4652 triangular elements (triangle side length of 6 mm) with a linear potential approach on each triangle [20] were used. The extent of the BEM model was approximately two times larger than the extent of the array of measuring points chosen. In the area where the highest potential gradients were expected, a local refinement was applied and the triangle side length was approximately halved. Fig. 5 shows the BEM model and the position of the measuring points.

We neglected the effect of the pipe wall curvature, which might be a potential source of error. However, the sensor grid and the pipe wall have a similar curvature, and we thus maintain the correct distance of the sensors with respect to each other and

to the pipe wall. Note that the diameter of the pipe was 610 mm and the distance between sensors and the pipe wall was 3.5 mm for the B_z sensors and 6 mm for the B_ρ sensors. Therefore, we do not expect a significant influence of the pipe wall curvature on our results.

D. Inverse Solution

For our inverse solutions, we use a general Bayesian framework that allows us to incorporate *a priori* information (e.g., [21], [22]).

We define:

m	measured data.
m_f	forward calculated data.
j	current dipole moments.
L	lead field matrix (kernel matrix).

For given source locations, the lead field matrix L links the dipole component vector j with the forward calculated data vector m_f

$$m_f = Lj. \quad (2)$$

For optimal source parameters, the squared deviation Δ^2 between the measured data m and the forward calculated data m_f is computed and minimized

$$\Delta^2 = \|m_f - m\|^2 = \|Lj - m\|^2. \quad (3)$$

Since the problem is ill-posed, regularization is needed. Regularization adds a second term, the model term $M(j)$, multiplied by the regularization factor λ

$$\Delta^2 = \|Lj - m\|^2 + \lambda \|Wj\|^2 = D(j) + \lambda M(j) \quad (4)$$

where W is the weighting matrix. The weighting matrix allows the incorporation of additional constraints such as source position weighting [22], [23].

In this paper, we apply and compare three different inverse algorithms: the L_p norm [22], [24], the maximum entropy method (MEM) [25], and the low resolution tomography (LORETA) [26].

In the L_p norm, data and modeling term are defined by

$$D(j) = \|Lj - m\|_{p_d} \quad \text{and} \quad M(j) = \|Wj\|_{p_m} \quad (5)$$

with $1 \leq p_d, p_m \leq 2$. The L_1 norm with $p_d = p_m = 1$ and the L_2 norm with $p_d = p_m = 2$ represent special cases. The L_2 norm is most widely used and also called minimum norm least squares (MNLS) [8], [9], [22].

LORETA uses a Laplacian coupling matrix B in the modeling term

$$M(j) = \|BWj\|^2. \quad (6)$$

The data term is according to (4). LORETA always reconstructs the smoothest of all possible source distributions. Although it is possible to use other norms, we apply only the L_2 norm in combination with LORETA.

The MEM uses an entropy measure as the model term

$$M(j) = \sum_{i=1}^N w_i \cdot |j_i| \cdot \log(\beta w_i \cdot |j_i|) \quad (7)$$

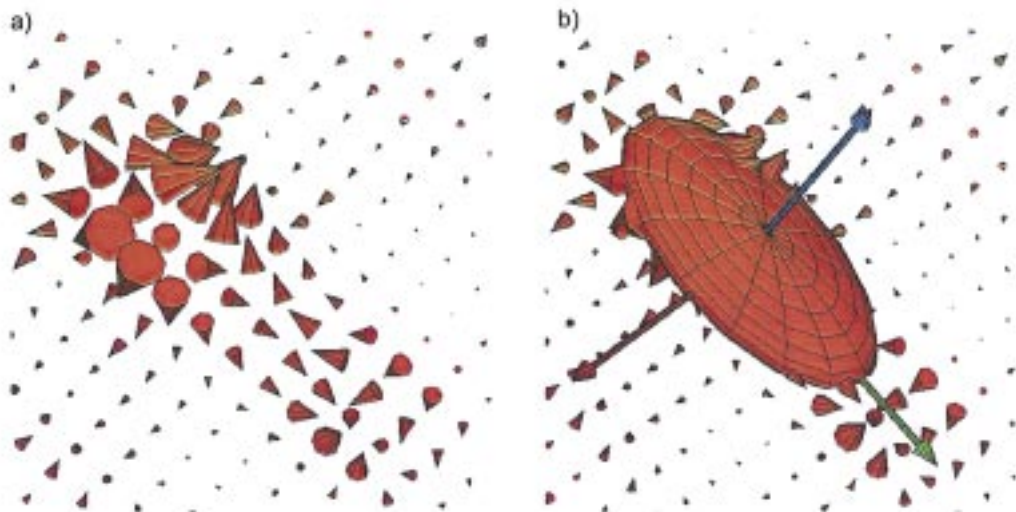


Fig. 6. (a) Current distribution obtained by the L_2 norm algorithm. (b) Equivalent ellipsoid fitted to this distribution. The cones indicate dipoles, where the size of a cone corresponds to the amplitude (strength) of a dipole. The direction of the dipole is indicated by the tip of the cone.

where N indicates the dimension of the lead field matrix and β can be related to a predefined unit current. The data term is again according to (4) with the L_2 norm. A detailed treatment of the implementation of MEM is given in [27].

The regularization parameter λ was estimated using the L -curve method [28]. Since this method failed in a number of cases, we also varied λ manually in order to assess its influence on the reconstructed results. λ was varied in steps of decimal power. The final values for λ were 1 or 10 for the L_1 norm, 0.1, 1, or 10 for MEM, and 10^{-6} , 10^{-5} , or 10^{-4} for the L_2 norm.

In contrast to the singular value decomposition (SVD) truncation scheme used in [8], [9], we apply a down weighting scheme of the lead field matrix as described in [22].

E. Computational Parameters

The source (dipole) positions were predefined on a quadratic grid with an extent of approximately 105 mm \times 105 mm, which was located below the array of the measuring points in the middle of the BEM model. In a first step, the minimum number of dipoles necessary for stable reconstruction results was estimated. Based on these estimates, we defined a grid of 52 \times 52 dipoles with a spacing of 2 mm for the small flaws (3, 5, 10, or 16 mm flaw diameter) and a grid of 21 \times 21 dipoles with a spacing of 5 mm for the large flaws (24 mm or 36 mm flaw diameter) [please compare Fig. 7(b) and (d) for the different grid sizes]. Please note that the different grids were introduced for the sake of reduced computation time. Grid spacing, as long as the grid is dense enough, is not expected to have a major influence on the solution [29].

For the sake of statistical comparison of the source reconstruction results and in order to reduce the large number of dipole parameters, we employed an equivalent ellipsoid approach detailed in [30]. An equivalent ellipsoid is defined as a three-dimensional ellipsoidal object fitted to a certain thresholded vector field (here a current distribution). The threshold T_h used for marking the most important region was defined empirically by $T_h = 100\% * (Q_{\max} + Q_{\text{mean}})/2Q_{\max}$, with

Q_{\max} being the maximum and Q_{mean} being the mean value of the dipole moments in the current distribution. Only dipoles having a dipole moment greater than the threshold T_h are used for fitting of the equivalent ellipsoid. The center of gravity of the thresholded region was computed, and the two semi-axes of the ellipsoid lying in the source reconstruction plane were calculated using the weighted longest dipole distance from the center of gravity. The weighting of the distance was done by the dipole moment in order to avoid that small and far-off dipoles have a large influence on the definition of the main axis. The third semi-axis was set to a fixed value since only dipoles in a plane were considered. With the help of this method, we estimated both the location and the extent of the flaws. Fig. 6 shows an example of a current distribution and the fitted equivalent ellipsoid.

Forward and inverse modeling were performed using the software CURRY, version 3.0 (Neuroscan Inc., Sterling, VA) running on a Sun UltraSparc 2 computer.

III. RESULTS

A. Evaluation of Algorithms

In a first evaluation, we tested all algorithms and source reconstruction parameters using three selected flaws and two criteria to assess the quality of the reconstruction process. The first criterion was that the reconstructed dipole distribution had to yield a clear focus with the maximum of the activity in the region of the flaw [please compare Fig. 7(a) and (b)]. The second criterion was $\Delta \leq 10\%$ (3). Based on these criteria, all reconstruction results using LORETA had to be rejected. Therefore, LORETA was not considered further in this study. Fig. 7 displays results of the four source reconstruction procedures tested.

B. Optimization of Parameters

The solution of the nonlinear reconstruction based on the L_p norm did not converge for different p in the data and in the model term (i.e., $p_d \neq p_m$). In the case $p = p_d = p_m$ similar results

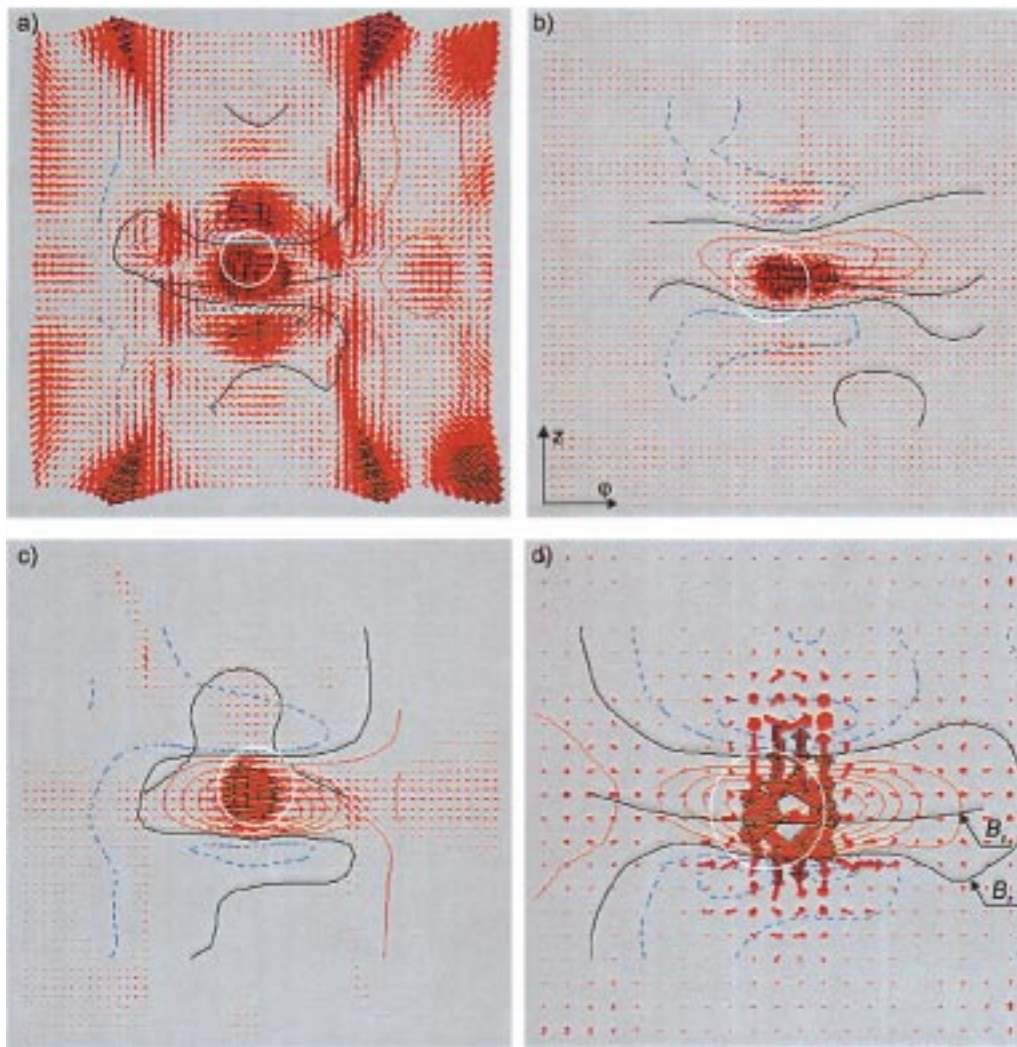


Fig. 7. Reconstruction results for (a) an internal flaw with 10 cm diameter and 50% depth using LORETA, (b) for an internal flaw with 16 cm diameter and 50% depth using MEM, (c) for an internal flaw with 16 cm diameter and 20% depth using the L_1 norm, and (d) for an internal flaw with 24 cm diameter and 50% depth using the L_2 norm. Red arrows indicate reconstructed dipoles, where the largest 20% of all dipoles are drawn with black borders. The white line depicts the actual flaw size. The magnetic field profile is plotted with blue (negative) and red (positive) lines, where the zero line is black. In (d), the zero lines are indicated for both B_z and B_ρ .

were obtained for $p \in \{1, 1.25, 1.5, 1.75, 2\}$. Thus, in the following only $p_d = p_m = 1$ and $p_d = p_m = 2$ (i.e., the L_1 and the L_2 norm) will be considered.

The reconstruction parameter λ was varied manually in a logarithmic scheme for all 20 flaws investigated since the L -curve method failed to produce meaningful results in a number of cases. An example of such a λ variation is presented in Fig. 8.

The minimum estimation error of the extent for all flaws was determined. The value of λ corresponding to this minimum error was 2.0 ± 3.6 for MEM, 7.2 ± 4.3 for the L_1 norm, and $6.0 \cdot 10^{-4} \pm 2.2 \cdot 10^{-3}$ for the L_2 norm (mean \pm standard deviation). For these values of λ , the deviation Δ was on average $42\% \pm 15\%$ for MEM, $46\% \pm 16\%$ for the L_1 norm, and $3.4\% \pm 3.6\%$ for the L_2 norm.

C. Estimation of Flaw Location

Fig. 9 gives the results of the location estimation errors which were determined by the difference of the flaw center points and the centers of gravity of the calculated equivalent ellipsoids.

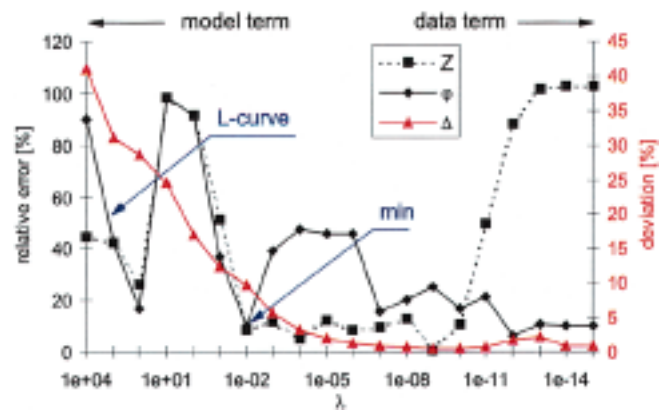


Fig. 8. Relative estimation error of the flaw extent and deviation Δ as a function of the regularization parameter λ . The results are based on the flaw with the largest diameter (SNR of $B_z = 21.4$, SNR of $B_\rho = 116.4$) and were calculated with the L_2 norm. The L -curve method computed an optimum at $\lambda = 1653$ while the minimum error (with regard to both directions z and φ) was obtained with $\lambda = 0.01$ (blue arrows). The legend above the diagram indicates the main influence of λ : the larger λ , the more the model term (i.e., the assumptions about the solution) is weighted [see (4)].

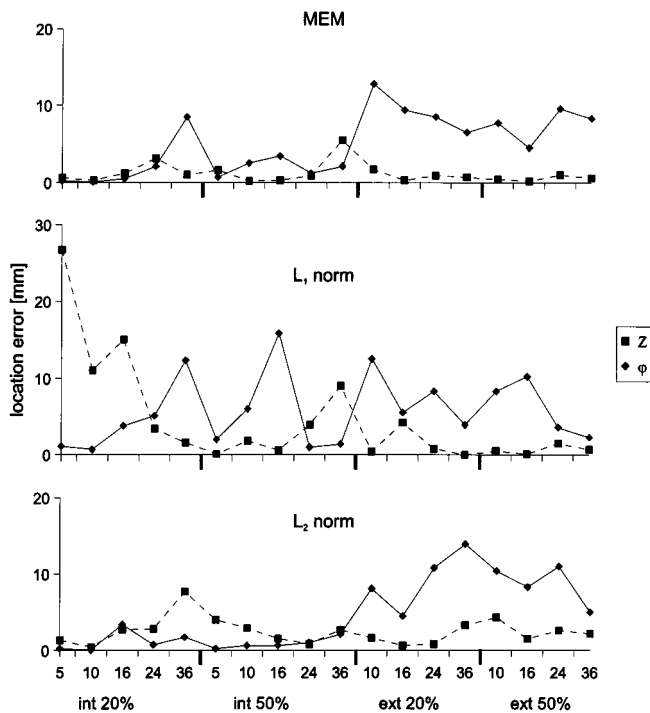


Fig. 9. Flaw location estimation error in both coordinate directions (z, φ) for different flaw diameters and positions (int: internal, ext: external).

For the external flaws, the location error was significantly higher in circumferential direction than in axial direction. For example, for the external flaws and the L_2 norm, the mean error in z direction was $2.1 \text{ mm} \pm 1.3 \text{ mm}$ and in φ direction $9.0 \text{ mm} \pm 3.2 \text{ mm}$. The results based on the L_1 norm exhibited the largest errors for the internal flaws (compared to the L_2 norm and MEM).

D. Estimation of Flaw Extent

Tables I–III show the estimated flaw extent for all methods and all flaws. These values are based on the semi-axes of the equivalent ellipsoids fitted to the current distribution as explained above.

For small flaws (5 or 10 mm diameter), MEM gave the best results, while for flaw diameters of 16 or 24 mm, the L_1 norm performed better and for the largest flaw (36 mm diameter), the L_2 norm was the best. For the L_1 norm, the circumferential direction φ was more accurately estimated than the axial direction z . The average performance was similar for all three algorithms.

IV. DISCUSSION

We applied and evaluated linear and nonlinear inverse algorithms in the analysis of measured MFL data with known flaw properties. One algorithm (LORETA) did not yield reasonable results and we suspect that the constraint underlying this algorithm, namely the smoothness of the solution, is not valid for MFL data. The other algorithms showed, on average, a similar performance in the flaw extent estimation. However, there was a tendency that MEM and the L_1 norm yield better results for smaller flaws while the L_2 norm is better for larger flaws. The errors of the flaw location estimation were comparable for

TABLE I
ESTIMATED FLAW EXTENT BASED ON MEM IN MM

		flaw diameter [mm]				
		5	10	16	24	36
internal	z	5.0	11.2	14.6	22.8	39.6
20%	φ	13.8	9.6	17.6	19.0	20.0
internal	z	6.2	9.2	22.2	26.0	42.4
50%	φ	5.0	10.8	16.6	17.4	33.2
external	z	—	10.0	15.6	24.0	55.8
20%	φ	—	15.0	18.6	20.0	34.2
external	z	—	10.6	17.2	26.2	33.8
50%	φ	—	10.6	5.2	21.8	11.2

TABLE II
ESTIMATED FLAW EXTENT BASED ON THE L_1 NORM IN MM

		flaw diameter [mm]				
		5	10	16	24	36
internal	z	4.8	9.0	13.8	24.0	34.4
20%	φ	4.8	26.2	16.8	12.0	15.2
internal	z	5.2	10.4	17.0	23.2	37.0
50%	φ	12.4	7.4	7.8	14.4	34.2
external	z	—	10.6	14.2	23.0	36.6
20%	φ	—	16.8	27.6	26.0	18.2
external	z	—	8.2	17.4	24.6	36.4
50%	φ	—	11.6	10.8	22.4	38.6

TABLE III
ESTIMATED FLAW EXTENT BASED ON THE L_2 NORM IN MM

		flaw diameter [mm]				
		5	10	16	24	36
internal	z	5.2	9.8	16.2	27.0	24.8
20%	φ	10.4	17.2	16.2	24.0	38.6
internal	z	15.0	9.4	14.6	23.6	32.4
50%	φ	8.8	7.0	26.2	35.4	39.0
external	z	—	7.0	15.2	22.6	38.2
20%	φ	—	9.4	25.6	25.4	35.6
external	z	—	10.6	19.0	28.8	38.8
50%	φ	—	9.4	16.6	25.6	35.8

MEM and the L_2 norm while the L_1 norm performed worse for those flaws situated on the internal pipe wall.

Due to its straightforward implementation and the low computational effort required, the L_2 norm has been used previously in the field of MFL data analysis [8]–[10]. Our results based on the L_2 norm share the same principal properties with those previous results, namely the robustness of the solution even for low SNR and the tendency to not very focused (i.e., smeared) distributions of the dipolar sources. The latter property is most probably the reason for the inferior performance of the L_2 norm on flaws with smaller diameter. We found that the L -curve method [28] failed to yield optimal values for the regularization parameter λ in a number of cases. Therefore, modifications of the L -curve method or different λ estimation methods [10] should be investigated in future studies.

Due to the fact that the measurement data included only two different flaw depths (20% or 50% of pipe wall thickness), we were not able to reliably assess the performance of the algorithms with regard to the estimation of the flaw depth. However, the mean dipole strength could be used in future studies to distinguish different flaw depths (Fig. 10). The information

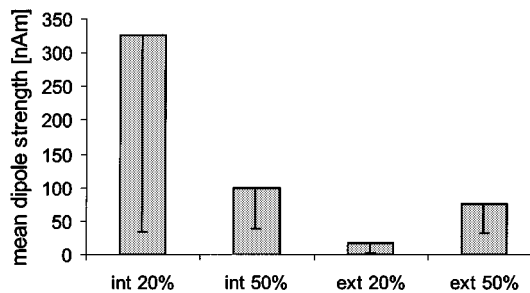


Fig. 10. Mean dipole strength from the L_2 norm reconstruction for different flaw depths (20% or 50% of wall thickness) and positions (int: internal, ext: external). The mean dipole strength is computed from all dipoles and subsequently averaged for all flaw diameters (5, 10, 16, 24, and 36 mm). The standard deviations are indicated by the error bars.

whether the flaw is located on the inside or outside of the wall is known *a priori* from the measurements. This *a priori* knowledge could be used in the estimation of the flaw depth based on the mean dipole strength. Yet another possibility for future applications is the use the Bayesian framework in order to incorporate the *a priori* knowledge about the position of the flaw (internal or external).

Although not shown explicitly in this paper, we found that the combination of both B_z and B_ρ yielded in general smaller errors in the estimation of flaw location and extent. Reconstructions based solely on B_ρ produced instable results with estimation errors of up to several hundred percent. This was probably caused by the lower spatial sampling in circumferential direction. Reconstructions based solely on B_z gave better results than those based solely on B_ρ , but performed worse than the combination of both. Besides the larger number of channels (i.e., input information) when using both B_z and B_ρ , we speculate that also the different information content based on the different spatial direction of the sensors contributes to the superior performance. An indication for this can be seen in Fig. 7, where the zero lines of the magnetic field profiles of B_z and B_ρ are depicted.

In a number of cases, we found a better estimation of the flaw location in z than in φ direction (Fig. 9), while the estimation of the flaw extent was better in φ than in z direction (Tables I–III). This is an unexpected result since the sampling in z direction is much denser than in φ direction (Fig. 3). Possible explanations for this finding may be the model assumptions of the inverse procedures, the spacing of the dipolar source grid, and the fact that only flaws with a circular shape were investigated.

There are some limitations in this study. For example, we neglected the effect of probe velocity. According to the literature, the effects of the probe velocity known so far are minor [31], [32]. Hysteresis effects are not taken into account in our computations because the applied magnetic field strength brings us well into the saturation part of the hysteresis curve. Other causes of error may be fluctuations in the calibration of the sensors and uncertainties in the lift-off geometry.

A recent study [33] investigated the influence of the boundary element discretization on the neuromagnetic forward and inverse problem. The authors found, that in order to reach acceptable localization errors, the ratio of the dipole distance to the surface and the triangle side length must not be less than 0.5. Furthermore, the overall triangle side length must be less than

10 mm. In this paper, the BEM resolution used for all calculations was 7 mm, thus fulfilling these two requirements for all dipole positions.

The computation of the noise level in the MFL data is of crucial importance for the inverse calculations, since all source reconstructions are carried out in the signal-to-noise space. The method used in this paper could probably be improved by adding more data to the noise level estimation (i.e., more statistical power) which in turn would also improve the source reconstruction. The SNR values for the flaws situated on the external wall with a depth of 20% (Fig. 4) do not exhibit large changes in SNR with increasing flaw diameter. This can be explained by the larger distance between the sensors and the flaws [34].

The computational effort for such a detailed analysis of MFL data as presented in this paper does not allow a real-time continuous data stream analysis. The inverse computations, however, can be performed on a standard desktop computer in a few seconds or a few minutes depending on the method chosen. Given the good performance of the algorithms evaluated in our study, it seems worthwhile to apply inverse algorithms in the analysis of MFL data.

V. CONCLUSION

The inverse algorithms based on MEM, the L_1 norm, and the L_2 norm are suitable for inverse computation of flaw extent and location in MFL data analysis. LORETA is not suitable for the analysis of MFL data. The L_2 norm seems more robust, requires less computation time, and is easier to implement than the other methods. Inverse algorithms potentially provide a powerful means for the detection and characterization of flaws in MFL data analysis.

REFERENCES

- [1] F. Foerster, "Nondestructive inspection by the method of magnetic leakage fields. Theoretical and experimental foundations of the detection of surface cracks of finite and infinite depth," *Defektoskopiya*, vol. 18, pp. 3–25, 1982.
- [2] —, "On the way from the know-how to the know-why in the magnetic leakage field method of nondestructive testing (part one)," *Mater. Eval.*, vol. 43, pp. 1154–1155, 1985.
- [3] Y. Zhang, K. Sekine, and S. Watanabe, "Magnetic leakage field due to sub-surface defects in ferromagnetic specimens," *NDT & E Int.*, vol. 28, pp. 67–71, 1995.
- [4] C. Edwards and S. B. Palmer, "The magnetic leakage field of surface-breaking cracks," *J. Phys. D: Appl. Phys.*, vol. 19, pp. 657–673, 1986.
- [5] L. N. Krotov, A. S. Shleenkov, R. S. Melnik, and V. E. Shcherbinin, "Computer modeling of magnetic fields of defects. The two-dimensional problem," *Rus. J. Nondestruct. Test.*, vol. 31, pp. 671–675, 1995.
- [6] W. Lord, J. M. Bridges, W. Yen, and R. Palanisamy, "Residual and active leakage fields around defects in ferromagnetic materials," *Mater Eval.*, vol. 36, pp. 47–54, 1978.
- [7] S. Ratnajeevan, "Inverse problem methodology and finite elements in the identification of cracks, sources, materials, and their geometry in inaccessible locations," *IEEE Trans. Magn.*, vol. 27, pp. 3433–3443, May 1991.
- [8] A. C. Bruno, "Imaging flaws in magnetically permeable structures using the truncated generalized inverse on leakage fields," *J. Appl. Phys.*, vol. 82, pp. 5899–5906, 1997.
- [9] A. C. Bruno, L. C. Miranda, C. H. Barbarosa, and G. S. Kühner, "Image reconstruction of spherical inclusions in ferromagnetic structures using the generalized inverse," *IEEE Trans. Magn.*, vol. 34, pp. 2912–2915, Sept. 1998.
- [10] G. McFall and R. Miracky, "A noise-tolerant solution to the magneto-static inverse problem for nondestructive evaluation," *J. Appl. Phys.*, vol. 74, pp. 2036–2045, 1993.

- [11] K. Miyata, K. Miya, and T. Sugira, "Crack shape recognition based on T-method," in *9th Int. Conf. Nondestructive Evaluation in the Nuclear Industry*, 1988, pp. 351–356.
- [12] K. Hanasaki and K. Tsukada, "Application of image restoration filter to two-dimensional measurements of magnetic flux leakage field around a surface flaw," in *1st U.S.-Jpn. Symp. Advances in Nondestructive Testing*, 1996, pp. 183–186.
- [13] S. Leonard and D. L. Atherton, "Calculations of the effects of anisotropy on magnetic flux leakage detector signals," *IEEE Trans. Magn.*, vol. 32, pp. 1905–1909, May 1996.
- [14] P. A. Ivanov, V. Zhang, C. H. Yeoh, L. Udpa, Y. Sun, S. S. Udpa, and W. Lord, "Magnetic flux leakage modeling for mechanical damage in transmission pipelines," *IEEE Trans. Magn.*, vol. 34, pp. 3020–3023, Sept. 1998.
- [15] L. Udpa, S. Mandayam, S. Udpa, Y. Sun, and W. Lord, "Development in gas pipeline inspection technology," *Mater. Eval.*, vol. 54, pp. 467–472, 1996.
- [16] K. Pesola, U. Tenner, J. Nenonen, P. Endt, H. Brauer, U. Leder, and T. Katila, "Multichannel magnetocardiographic measurements with a physical thorax phantom," *Med. Biol. Eng. Comput.*, vol. 37, pp. 2–7, 1999.
- [17] D. Craik, *Magnetism: Principles and Applications*. Chichester, U.K.: Wiley, 1995.
- [18] H. Hofmann, *Das elektromagnetische Feld*. Berlin, Germany: Springer, 1986.
- [19] P. Lorrain, D. R. Corson, and F. Lorrain, *Electromagnetic Fields and Waves*, 3rd ed. New York: Freeman, 1988.
- [20] M. Fuchs, R. Drenckhahn, H. A. Wischmann, and M. Wagner, "An improved boundary element method for realistic volume conductor modeling," *IEEE Trans. Biomed. Eng.*, vol. 45, pp. 980–997, Aug. 1998.
- [21] D. M. Schmidt, J. S. George, and C. C. Wood, "Bayesian inference applied to the electromagnetic inverse problem," *Hum. Brain Map.*, vol. 7, pp. 195–212, 1999.
- [22] M. Wagner, "Rekonstruktion neuronaler Ströme aus bioelektrischen und biomagnetischen Messungen auf der aus MR-Bildern segmentierten Hirnrinde," Ph.D. dissertation, Techn. Univ. Hamburg-Harburg, 1998.
- [23] M. Fuchs, M. Wagner, T. Köhler, and H. A. Wischmann, "Linear and nonlinear current density reconstructions," *J. Clin. Neurophysiol.*, vol. 16, pp. 267–295, 1999.
- [24] K. Matsuura and Y. Okabe, "Selective minimum-norm solution of the biomagnetic inverse problem," *IEEE Trans. Biomed. Eng.*, vol. 42, pp. 608–615, June 1995.
- [25] M. Huang, R. Aron, and C. A. Shiffman, "Maximum entropy method for magnetoencephalography," *IEEE Trans. Biomed. Eng.*, vol. 44, pp. 98–102, Jan. 1997.
- [26] R. D. Pascual-Marqui, "LORETA in 3D solution space," *ISBET Newsletter*, vol. 6, pp. 22–28, 1995.
- [27] T. Köhler, A. Theißen, M. Wagner, H.-A. Wischmann, and M. Fuchs, "Maximum entropy in current density imaging," *Biomed. Tech.*, vol. 42, pp. 49–52, 1997. Suppl. 1.
- [28] P. C. Hansen, "Analysis of discrete ill-posed problems by means of the L-curve," *SIAM Rev.*, vol. 34, pp. 561–580, 1992.
- [29] U. Tenner, "Source modeling in cardiomagnetism: A physical torso phantom for biomagnetic and bioelectric heart field measurements," Ph.D. dissertation, Techn. Univ. Ilmenau, 2001.
- [30] M. Ziólkowski, J. Haueisen, H. Nowak, and H. Brauer, "Equivalent ellipsoid as an interpretation tool of extended current distributions in biomagnetic inverse problems," *IEEE Trans. Magn.*, vol. 36, pp. 1692–1695, July 2000.
- [31] Y. S. Sun, "Influences of velocity on signal responses of magnetostatic nondestructive testing tools: A prediction from finite element analysis," *IEEE Trans. Magn.*, vol. 30, pp. 3308–3311, Sept. 1994.
- [32] Y. K. Shin and W. Lord, "Numerical modeling of moving probe effects for electromagnetic nondestructive evaluation," *IEEE Trans. Magn.*, vol. 29, pp. 1865–1868, Mar. 1993.
- [33] J. Haueisen, A. Böttner, M. Funke, H. Brauer, and H. Nowak, "Influence of boundary element discretization on the forward and inverse problem in electroencephalography and magnetoencephalography," *Biomed. Tech.*, vol. 42, pp. 240–248, 1997.
- [34] F. Foerster, "New findings in the field of nondestructive magnetic leakage field inspection," *NDT Int.*, vol. 19, pp. 3–14, 1986.